

Nickel ferrite/TiO₂ Nanofibrous Composite: Enhanced Photocatalytic Dye Degradation Under Visible Light

Hellen C. T. Firmino^{a,b,*} , Emanuel P. Nascimento^{a,b}, Rondinele N. Araujo^{a,b}, Francisco J.A. Loureiro^c,
Gelmires A. Neves^{a,b}, Marco A. Morales^d, Romualdo R. Menezes^{a,b}

^aUniversidade Federal de Campina Grande, Departamento de Engenharia de Materiais, Laboratório de Tecnologia de Materiais, Campina Grande, PB, Brasil.

^bUniversidade Federal de Campina Grande, Programa de Pós-Graduação em Ciência e Engenharia de Materiais, Campina Grande, PB, Brasil.

^cUniversidade de Aveiro, Centro de Tecnologia Mecânica e Automação, Departamento de Engenharia Mecânica, Laboratório Associado de Sistemas Inteligentes, Guimarães, Portugal.

^dUniversidade Federal do Rio Grande do Norte, Departamento de Física Teórica e Experimental, 59078-970, Natal, RN, Brasil.

Received: June 9, 2023; Revised: November 24, 2023; Accepted: January 16, 2024

A highly efficient NiFe₂O₄/TiO₂ nanofibrous photocatalyst was prepared by a simultaneous solution spinning method. The hybrid fibers were characterized by scanning electron microscopy (SEM), X-ray diffraction (XRD), Raman spectroscopy, and magnetometry. The photocatalytic properties were evaluated using Crystal violet (CV) and Congo red (CR) dyes under visible light irradiation. Fibers calcined at 600 °C and 700 °C showed the highest CV decolorization (77%). On the other hand, for CR, the best performance was encountered with the photocatalysts heat-treated at 500 °C, which exhibited photocatalytic degradation of 87% after only 30 min of visible light irradiation. The high reaction rates (0.018 to 0.067 min⁻¹) explain the fast decolorization yielded by the combined effect of adsorption and photocatalytic processes. Moreover, recyclability assays showed stable CR dye efficiency after five recycling cycles. Therefore, the NiFe₂O₄/TiO₂ nanofibers present a high potential for application in the decolorization treatment of wastewater from the textile industry.

Keywords: Nickel ferrite/titania nanofibers, Congo red, Crystal violet, Photocatalysis.

1. Introduction

The tenacious contamination of water bodies by non-biodegradable industrial dye effluents is a major environmental issue. The problem is aggravated by the growing population and accelerated industrial development that increases the dumping of toxic, carcinogenic, or mutagenic compounds, endangering all living creatures¹⁻³. Many methods are employed to clean water polluted with colored industrial effluents, such as coagulation and flocculation⁴, precipitation, adsorption⁵, and photocatalytic processes⁶. The difficulty of separating and reusing the photocatalytic material complicates the use of most methods. Therefore, the demand for magnetic photocatalysts has increased because they allow facile materials recovery by simple routes, such as magnetic separation^{7,8}.

The photocatalytic process involves the use of a light source (UV, visible) and a light-active material to promote the formation of active free radicals ($\bullet\text{OH}$, $\text{O}_2^{\bullet-}$) that degrade organic dyes into CO₂, H₂O, and other less toxic byproducts³. Many magnetic and non-magnetic materials are suitable as photocatalysts, such as $\alpha\text{-Fe}_2\text{O}_3$ ⁶, Fe₃O₄⁹, MnFe₂O₄^{10,11}, CoFe₂O₄¹², (Zn_{1-x}Ge)(N₂O_x)¹³, gallium oxynitride (GaON)¹⁴, and N-doped La₃Ti₂O₇¹⁵. These materials have narrow band gaps that allow electron excitation from the valence band

(VB) to the conduction band (CB), forming electron-hole pairs fundamental at producing active free radicals in aqueous media. Additionally, organic dyes can adsorb onto ferrites and further enhance the removal effectiveness⁷. However, occasionally their photocatalytic properties are limited by electron-hole recombination.

To avoid recombination, nano-hybrids and nanocomposites between ferrite, and other semiconductors have been developed for photocatalytic/adsorptive systems. Zhu, Jiang⁷ reported the simultaneous adsorption/photocatalytic removal of Congo red dye by Fe₃O₄/Bi₂S₃ microspheres. They achieved 85% CR removal after 90 min of the experiment. TiO₂/CNTs@CoFe₂O₄ prepared by Sohail, Xue¹⁶ presented high photodegradation efficiency (96%) against methylene blue (MB) under UV light. Tariq, Fatima³ synthesized MoO₃/CoFe₃O₄ nanocomposites that exhibited 91%, 54%, and 65% photodegradation of methylene blue, rhodamine B, and crystal violet dyes after UV-visible light exposure. Manohar, Chintagumpala¹⁷ synthesized mixed Zn-Ni spinel ferrites for efficient photocatalytic degradation of methylene blue under visible light. The results show a 96% degradation of MB after 2 h of visible light irradiation. Dojcinovic, Vasiljevic¹⁸ reported the synthesis of efficient (82% degradation under 4 h of sunlight exposure) MB photocatalysts based on mixed Mg-Co spinel ferrites.

*e-mail: hellentorrano@hotmail.com

These works highlight the potential of such mixed materials as photocatalytic agents against harmful dyes. However, research is still lacking on new functional materials to decolorize waters contaminated with Crystal violet and Congo red dye, which are both carcinogenic and toxic¹⁹⁻²¹. Most of these prospective materials are synthesized as nanoparticles, which easily aggregate, decreasing their catalytic activity on the surface. Therefore, new morphologies less susceptible to self-aggregation should be explored to achieve optimized photocatalytic systems. To our understanding, there are no studies regarding the synthesis and photocatalytic properties of magnetic nickel ferrite/TiO₂ hybrid fibers. Micro- and nanofibers are interesting materials having many advantages, including a low tendency for aggregation, high specific surface properties, and high functionality.

Therefore, we synthesized hybrid NiFe₂O₄/TiO₂ fibers using the solution blow spinning (SBS) method²². The SBS emerged as an alternative method for efficient and high-productive fabrication of ceramic nanofibers^{6,23,24}. Photocatalytic degradation of Crystal violet and Congo red dyes was performed using visible light. After each experiment, the fibers were recovered, heat-treated, and subjected to new photocatalytic experiments to assess their recyclability. The structural and magnetic properties of the hybrid NiFe₂O₄/TiO₂ fibers were also studied.

2. Experimental

2.1. Materials

For fiber preparation, iron (III) nitrate nonahydrate ($\geq 98\%$, Sigma Aldrich, Brazil), nickel nitrate hexahydrate ($\geq 99\%$, Sigma Aldrich, Brazil), and titanium isopropoxide (TTIP, $\geq 97\%$, Sigma Aldrich, Brazil) were used as ceramic precursors. Polyvinylpyrrolidone (PVP, Mw~1,300,000 g/mol, Sigma Aldrich, Brazil) was added to aid fiber spinning. The solvents used were distilled water, acetic acid (99.7%, Dinâmica, Brazil), ethanol (99.5%, Dinâmica, Brazil), and dimethyl carbonate (DMC, $\geq 99\%$, Sigma Aldrich, Brazil).

2.2. Preparation of ferrite/TiO₂ fibers

Two distinct precursor solutions were prepared and spun simultaneously using two spinning systems²⁵, as detailed in Figure 1. The first precursor solution was prepared to

obtain the NiFe₂O₄ fibers, while the second produced the TiO₂ fibers. The preparation of the first solution followed two steps. In the first step, 2.01 g of iron nitrate and 0.58 g of nickel nitrate were dissolved in 1.25 mL of acetic acid. This solution remained under constant agitation for 2 hours. In the second step, 12 w/v% PVP was dissolved in distilled water, maintaining a 1:1 volumetric ratio between the acetic acid (first step) and the distilled water (second step). This solution was vigorously stirred until the complete dissolution of PVP. Finally, solution 1 was mixed with solution 2 and stirred for 2 hours to obtain the final NiFe₂O₄ solution.

The TiO₂ precursor solution was prepared as follows: 2 mL of titanium isopropoxide was dissolved in an ethanol/DMC mixture (1:1 volumetric ratio). After that, 0.2 mL of acetic acid was added to the solution, with constant stirring for 1 hour. Finally, 8 w/v% PVP was added to the solution, which was stirred for 1 hour. It is worth noting that the precursor solutions of NiFe₂O₄ and TiO₂ were separately prepared to produce a heterogeneous material composed of NiFe₂O₄ and TiO₂ fibers and study the interaction between these two components. Mixing the two precursor solutions in a single solution would not generate the intended interaction and would cause problems such as doping, impurity phases, and precipitation.

The final NiFe₂O₄ and TiO₂ solutions were placed into syringes and immediately spun using the spinning apparatus shown in Figure 1. The SBS system consists of two spinning nozzles connected to two injection pumps. A collector and a tubular oven heated to approximately 100 °C were employed to help dry the fibers as they formed. Feeding rates of 4.5 and 6.0 were applied to force-feed the nickel ferrite and titanium dioxide solutions through an inner nozzle. For both solutions, constant air pressure of 0.21 MPa was blown through an outer nozzle to drive fiber formation. The as-spun NiFe₂O₄/TiO₂ fibers were annealed for 2 h in a closed crucible using a muffle furnace operating with a 5 °C/min heating rate. The temperatures of calcination were 500, 600, and 700 °C. TiO₂ fibers were prepared under similar conditions and calcined at 500 °C for comparison. The final compositions were designated as TiO₂, NiFeTi500, NiFeTi600, and NiFeTi700.

2.3. Characterizations

The morphology of the post-annealed fibers was investigated by scanning electron microscopy (SEM) (TESCAN, VEGA3).

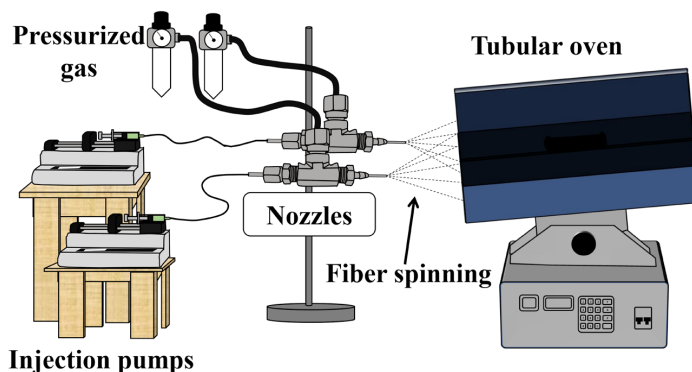


Figure 1. Schematic illustration of the SBS apparatus.

Fiber diameter was measured for ~100 fibers using the Image J software (National Institutes of Health, USA). X-ray diffraction (XRD) (Shimadzu, XRD-6000), using CuK α X-ray source (1.5818Å), and Raman spectroscopy (Renishaw inVia Raman spectrometer, excitation laser $\lambda = 785$ nm, laser power of 0.1% and 10 accumulations) were performed to study the structural properties. The XRD patterns were refined through the Rietveld method using MAUD software (Materials Analysis Using Diffraction). Magnetic measurements were performed using a vibrating sample magnetometer (VSM) (Lakeshore, model 7400) with a maximum magnetic field of ± 15 kOe and 80 Oe step field. All magnetic measurements were recorded at room temperature.

Crystal violet (CV) and Congo red (CR), two carcinogenic dyes, were employed in the photocatalytic experiments to study the performance of the hybrid ferrite/TiO₂ fibers against hard-to-degrade cationic (Crystal violet) and anionic (Congo red) dyes. The experiments were conducted at room temperature (25 °C) in triplicate using 5 mg/L CV or CR aqueous solutions at pH 7. For each experiment, 5 mg of the sample was dispersed in 10 mL of CV or CR dye solutions. The suspensions were kept under agitation in a shaker incubator (NT 735, Nova Técnica, Brazil) and exposed to visible light using incandescent lamps (200 W). At fixed intervals of 30 min, 5 mL aliquots of the suspensions were collected, centrifuged, and their concentration was determined by UV-Vis spectroscopy (Shimadzu, UV-1800) in the 400-800 nm range to find the degradation efficiency.

The typical absorption wavelength of CV and CR dye are $\lambda_{\text{max}} = 582$ and 501 nm, respectively.

3. Results and Discussion

The fibers present a continuous structure, round cross-section, and a rough surface that indicates porosity. The high-magnification images (Figure 2b, e, h) showed evidence of surface roughness. The heat-treated fibers exhibited mean diameters ranging from 675 ± 181 nm to 810 ± 176 nm. The large fiber diameter could be due to the high polymer concentration in the solution (12 w/v%) and the combined effect of low air pressure (~0.21 MPa) and large inner nozzle protruding distance (15 mm)²². There is also evidence of fiber adhesion between adjacent fibers, which is an inevitable process caused by difficulties in solvent evaporation and coalescence during heat treatment. In SBS, fiber diameter can be controlled mainly by changing gas pressure and polymer concentration. X-ray fluorescence mapping (Figure 2c, f, i) shows a uniform distribution of Ni, Fe, and Ti elements, indicating that the NiFe₂O₄ and TiO₂ fibers could be arranged in an intertwined way in the samples. It is also possible to distinguish fibers rich in Ti from fibers containing Ni and Fe. The presence of conjoined fibers in a fiber bundle may increase the chance of contact between ferrite and titania fibers, forming localized NiFe₂O₄/TiO₂ junctions. The interaction along the interface of continuous fibers of different natures could improve electron transport and facilitate the photocatalytic process.

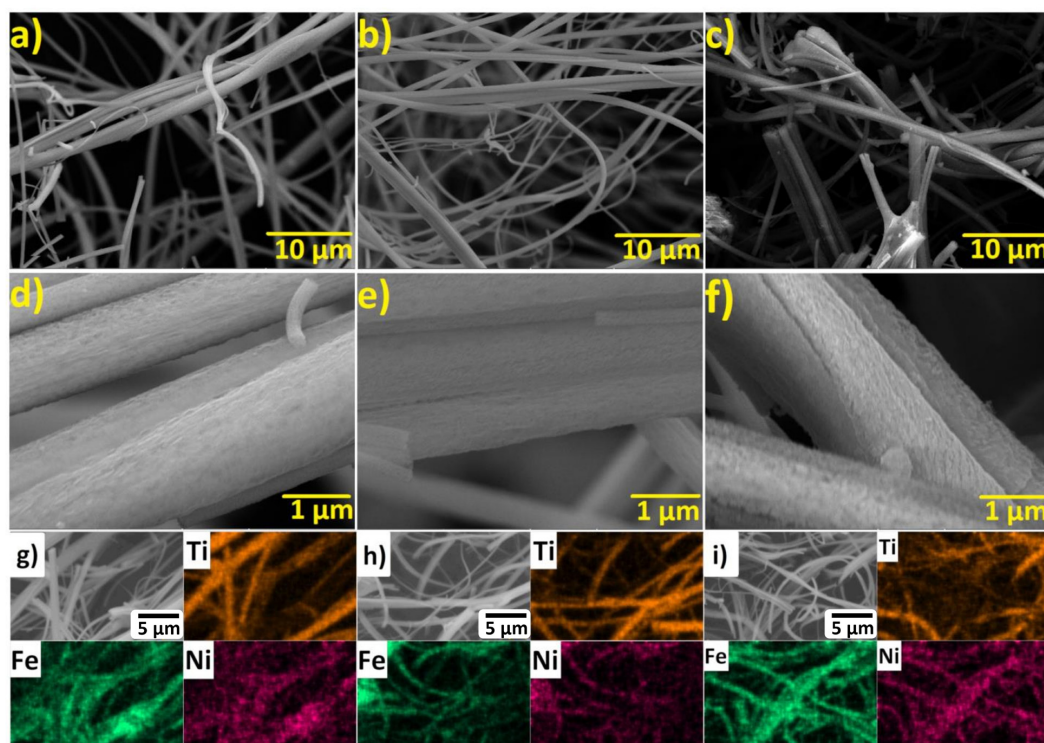


Figure 2. Low magnification SEM images (a, b, c) of NiFeTi500, NiFeTi600, and NiFeTi700 samples. High magnification SEM images (d, e, f) of the NiFeTi500, NiFeTi600, and NiFeTi700 compositions. X-ray fluorescence mapping (g, h, i) of NiFeTi500, NiFeTi600, and NiFeTi700 samples.

Figure 3 shows the X-ray diffraction results of the NiFeTi500, NiFeTi600, and NiFeTi700 fibers. The Rietveld refinement method was applied to estimate the structural parameters and phase concentration of the samples. Table 1 exhibits the lattice parameters, crystallite size, and percentage of phases for the NiFe₂O₄/TiO₂ hybrid fibers. The NiFeTi500 sample (calcined at 500 °C) showed characteristic peaks of the spinel-type nickel ferrite (COD 5910064) phase and the anatase phase of titanium dioxide (ICSD 9852). At higher temperatures, 600 °C and 700 °C, in addition to the spinel and anatase phases, hematite (ICSD 15840) and rutile-type (ICSD 9161) titanium dioxide phases appeared. Therefore, the heat treatment at 500 °C was enough to form the desired phases without the presence of iron oxide impurity phases. Besides, the anatase phase is metastable and, thus, more reactive and preferable for catalytic purposes²⁶. The formation of the rutile phase agrees with the anatase-to-rutile transition that is reported to take place between 600 °C and 700 °C in titania samples²⁷. The acidic media used in fiber preparation did not seem to favor rutile formation since acetic acid is a weak acid²⁶. As expected, the increase in calcination temperature led to grain size growth in all phases²⁶. The lattice parameters agree with the ICSD card files and suffer no influence from the calcination temperature. However, as the temperature increased, the amount of rutile phase incremented at the expense of other phases (Table 1).

Figure 4 presents the Raman spectra and the respective positions of the Raman bands for the NiFe₂O₄/TiO₂ fibers. The samples are constituted mainly of nickel ferrite and TiO₂; therefore, we expect to find Raman modes associated with these two constituents. Nickel ferrite is known to have an inverse spinel structure, with prototype symmetry O_h⁷ and space group *Fd* $\bar{3}$ *m*. In the Ni-ferrite structure, half of the Fe³⁺ cations occupy the tetrahedral A-site positions, and Ni²⁺ and the other half of the Fe³⁺ cations are distributed over the octahedral B-site locations²⁸. Therefore, 42 vibrational modes are predicted for the spinel structure of nickel ferrite according to group theory^{28,29}, which are represented as $\Gamma = A_{1g} + E_g + T_{1g} + 3T_{2g} + 2A_{2u} + 2E_u + 4T_{1u} + 2T_{2u}$. A_{1g}, E_g, and T_{2g} modes are Raman active, while the four T_{1u} are infrared (IR) active. The remaining vibrational modes are not IR and Raman active³⁰.

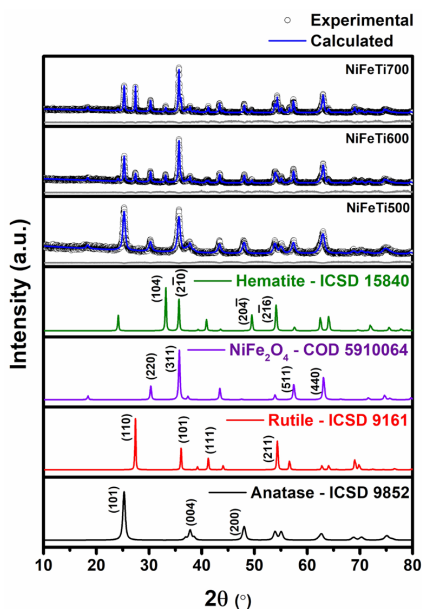


Figure 3. Rietveld refinement of X-ray diffraction patterns and simulated patterns obtained from ICSD cards.

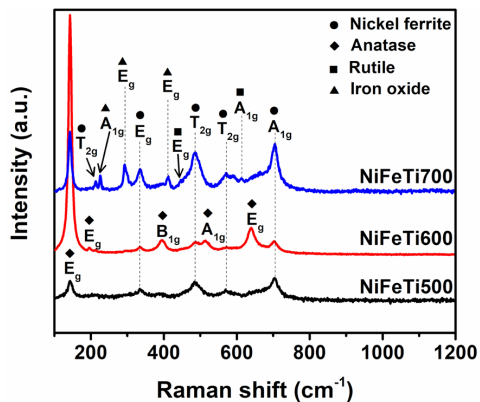


Figure 4. Raman spectra of the TiO₂/NiFe₂O₄ samples calcined at different temperatures.

Table 1. Structural parameters and concentrations obtained by the Rietveld refinement. The first rows show lattice parameters from CIF cards.

	Anatase – ICSD 9852			Rutilo – ICSD 9161			NiFe ₂ O ₄ – COD 5910064		αFe ₂ O ₃ – ICSD 15840		
Patterns	D (nm) [% of phase]	a (Å)	c (Å)	D (nm) [% of phase]	a (Å)	c (Å)	D (nm) [% of phase]	a (Å)	D (nm) [% of phase]	a (Å)	c (Å)
Anatase	----	37.842	95.146	----	----	----	----	----	----	----	----
Rutile	----	----	----	----	45.941	29.589	----	----	----	----	----
NiFe ₂ O ₄	----	----	----	----	----	----	8.337	----	----	----	----
α-Fe ₂ O ₃	----	----	----	----	----	----	----	----	----	5.038	13.772
Samples	D (nm) [% of phase]	a (Å)	c (Å)	D (nm) [% of phase]	a (Å)	c (Å)	D (nm) [mass % of phase]	a (Å)	D (nm) [% of phase]	a (Å)	c (Å)
NiFeTi500	24.47 [59.0%]	3.786	9.513	----	----	----	19.69 [40.6%]	8.341	----	----	----
NiFeTi600	63.43 [36.5%]	3.783	9.517	57.38 [16.3%]	4.592	2.959	53.61 [36.8%]	8.336	78.94 [10.34%]	5.035	13.757
NiFeTi700	70.4 [31.7%]	3.783	9.517	179.76 [28.0%]	4.592	2.959	66.59 [34.5%]	8.337	99.0 [5.73%]	5.036	13.744

On the other hand, titania has three distinct crystal structures (rutile, anatase, and brookite) and undergoes phase transformation depending on the ambient conditions. Rutile (thermodynamically stable) and anatase (metastable) are the main crystal structures of TiO₂. The anatase structure belongs to the tetragonal space group D_{4h}^{19} ($I4_1/amd$). According to group theory, there are six Raman active modes: $A_{1g} + 2B_{1g} + 3E_g$. Conversely, the rutile structure belongs to the $P42/mnm$ tetragonal space group, having five Raman active modes: B_{1g}, E_g, A_{1g} , and B_{2g} ³¹. Lastly, α -Fe₂O₃ shows two A_{1g} and five E_g Raman active modes³². Raman spectra of the NiFeTi500, NiFeTi600, and NiFeTi700 nanofibers (Figure 3) corroborated the XRD results.

Table 2 shows the Raman peaks and their corresponding descriptions. Raman shifts at 143 cm⁻¹, 195 cm⁻¹, 394 cm⁻¹, 513 cm⁻¹, and 639 cm⁻¹ presented in the samples are all assigned to the anatase phase of TiO₂. Only the NiFeTi700 presented two features at 445 cm⁻¹ and 613 cm⁻¹ related to the rutile-type structure. Although the XRD showed rutile formation at 600 °C, the low concentration (16% - Table 1) was not enough to be detected by Raman. However, the presence of rutile at 700 °C further corroborates the anatase-to-rutile transformation between 600 and 700 °C²⁷. The peaks at 213 cm⁻¹, 335 cm⁻¹, 487 cm⁻¹, 571 cm⁻¹, 663 cm⁻¹ (broad shoulder), and 705 cm⁻¹ are ascribed to the NiFe₂O₄ phase^{29,33,34}.

The Raman modes located in the 625-730 cm⁻¹ (A_{1g} band) region represent the tetragonal sites, a common feature of the cubic inverse-spinel ferrite structures³⁵. The vibrational modes in the 430-620 cm⁻¹ interval correspond to octahedral sites. This is in good agreement with the literature^{35,36}. The peaks at 225 cm⁻¹ (A_{1g} mode), 293 cm⁻¹, and 412 cm⁻¹ (E_g modes) belong to the hematite crystal structure³⁷.

Room temperature magnetic measurements were performed to investigate the magnetic response of the samples to an external field. Figure 5a shows room temperature M – H hysteresis loops. The samples exhibit a typical ferrimagnetic behavior.

The saturation magnetization (M_s), coercivity field (H_c), and remanence magnetization (M_r) are summarized in Table 3. The saturation magnetization was determined using the law of approach to saturation (LAS): $M = M_s(1-B/H^2)$, where B and M_s are fitting parameters³⁸, and M and H are the magnetization and the magnetic field, respectively. The method consists of plotting $M \times 1/H^2$ using the magnetization data for $H \geq 10^4$ Oe (i.e., $H \gg$ coercivity field (H_c)) and then fitting the experimental data to a linear function. M_s is obtained when $(1/H^2) \rightarrow 0$. Figure 5b-d exhibits M versus $1/H^2$ plots and their respective linear fittings for the samples. As one can note, all $M \times 1/H^2$ plots follow a linear trend indicating that the LAS equation is appropriate for our data.

Table 2. Main Raman shifts (cm⁻¹) of the phases observed for the samples and their assignment.

	NiFeTi500	NiFeTi600	NiFeTi700	Assignment
Anatase				
	143	143	143	Eg ³
	-	195	-	Eg ²
	394	392	-	B1g
	513	513	-	A1g
	634	639	-	Eg ¹
Rutile				
	-	-	445	Eg
	-	-	613	A1g
NiFe₂O₄				
	-	213	213	T2g ³
	335	335	335	Eg
	487	487	485	T2g ²
	571	564	571	T2g ¹
	703	705	705	A1g ¹
α-Fe₂O₃				
	-	225	225	A1g
	-	293	293	Eg
	-	-	412	Eg

Table 3. Magnetic parameters for NiFe₂O₄/TiO₂ nanofibers.

Sample	M_s (emu/g)	M_r (emu/g)	$R = M_r/M_s$	H_c (Oe)
NiTi500	18.8	2.2	0.12	110.0
NiTi600	20.4	5.3	0.26	178.0
NiTi700	20.4	5.5	0.27	178.0

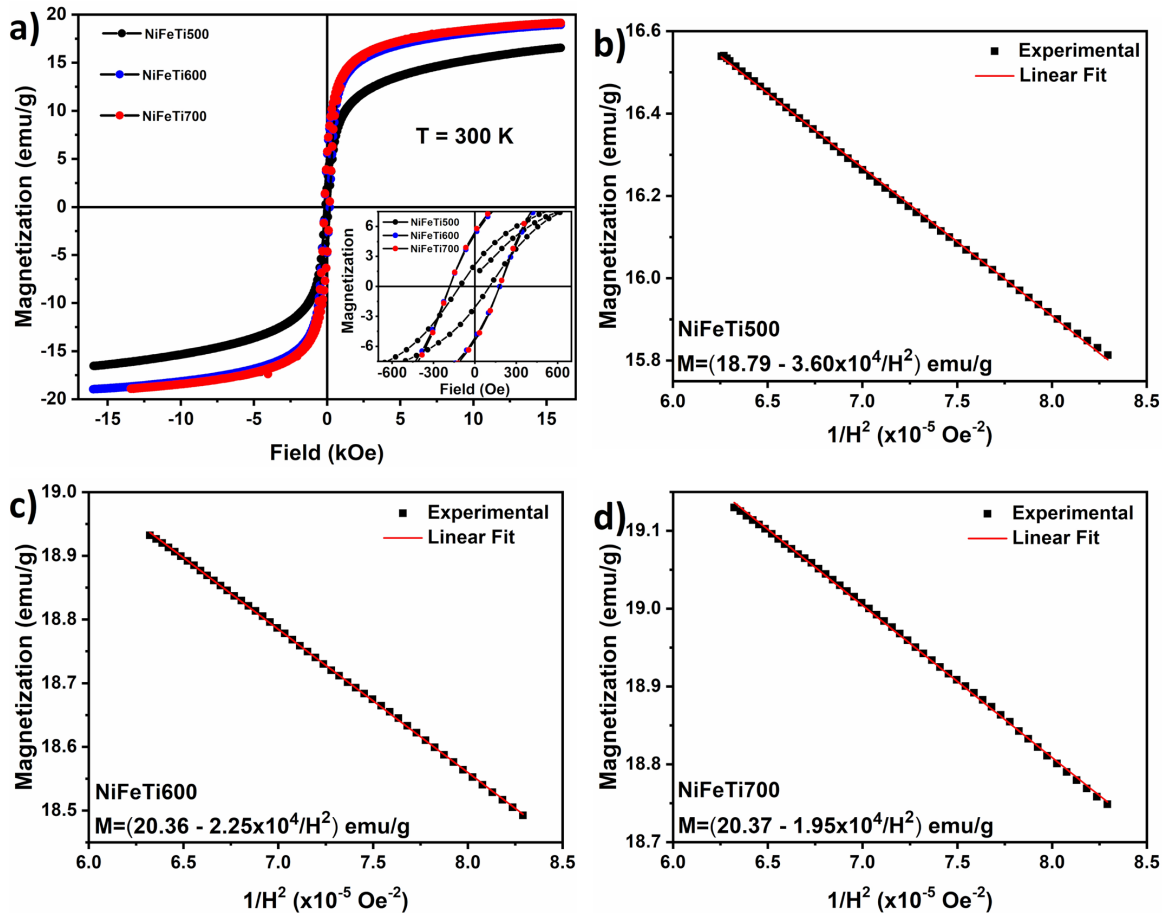


Figure 5. (a) Magnetic hysteresis at 300 K for all NiFe₂O₄/TiO₂ nanofibers. M vs. 1/H² plots and linear fits for samples NiFeTi500 (b), NiFeTi600 (c), and NiFeTi700 (d). Insets are the parameters obtained from the linear fittings.

The M_s values for the NiFeTi500, NiFeTi600, and NiFeTi700 samples were 18.79, 20.37, and 20.36 emu/g, respectively. These values are lower than the reported for bulk NiFe₂O₄ (55 emu/g)³⁹ due to the mass contribution of anatase and rutile nonmagnetic phases and the α -Fe₂O₃ antiferromagnetic phase. However, considering the mass percentage of NiFe₂O₄ obtained from the refinements, we can roughly calculate the actual magnetization of the NiFe₂O₄ phase, $M_{\text{NiFe2O4}} = M_s / \text{mass}\%$; therefore, the calculated values are 46, 55, and 58 emu/g. These values are in close agreement with bulk NiFe₂O₄. Furthermore, the M_s values found in this work are comparable and even higher than some results found in the literature for NiFe₂O₄ nanomaterials^{8,40,41}. The NiFe₂O₄/TiO₂ samples show a good response to an external magnetic field and, therefore, can be completely separated from a treated aqueous suspension using a magnet. Facile magnetic separation is advantageous in the design of systems to eliminate organic pollutants from industrial wastewater⁸.

The H_c at 300 K were 110 Oe, 178 Oe, and 178 Oe for NiFeTi500, NiFeTi600, and NiFeTi700 samples, respectively. Therefore, the coercivity increased upon increasing the calcination temperature from 500 °C to 700 °C. Coercivity is influenced by microstructural variations, such as strain,

cation defects, and magneto-crystalline anisotropy⁴¹. The XRD study shows that the average crystallite size increase with increasing calcination temperature. The increase in crystallite size could be responsible for the increment in coercivity, similar to what happens in single-domain particles wherein the coercivity is related to particle size³⁸. Also, the increase in calcination temperature promotes less distortion in the crystal lattice and contributes to higher coercivities. The angular coefficient ($M_s \times B$) obtained in the linear fittings using the LAS is related to magnetocrystalline anisotropy (K) through the equation $K = M_s \times B^{0.5} / (\rho \times A^{0.5})$, where ρ is the density of Ni-ferrite, A is a constant with values of 8/105 and 4/15 for samples with cubic or uniaxial magnetic anisotropy, respectively. Because the M_s values were obtained using the masses of Ni-ferrite and the masses of the second phases, we cannot calculate the K values. The B values were 1918, 1104, and 959 emu \times Oe²/g for samples NiFeTi500, NiFeTi600, and NiFeTi700.

The ratio (R) of remanent magnetization M_r and M_s increases with increasing calcination temperature (Table 3). R reflects the grain growth and the soft magnetic property of the samples. The M_r results found in this work are analogous to findings reported by Joshi, Kumar⁴¹ for Ni ferrite nanoparticles.

The optical properties of the NiFe₂O₄ and TiO₂ fibers were studied by UV-Vis diffuse reflectance. Band gap (E_g) values were determined using the modified Kubelka-Munk equation:

$$[F(R)hv]^n = B(h\nu - E_g) \quad (1)$$

where R is the reflectance, $F(R)$ is proportional to the absorption coefficient α , B is a constant, h is the Planck's constant (J.s), and ν represents the frequency of the UV light (s⁻¹). The interception between the extrapolated linear portion of the $[F(R)hv]^n$ vs. $h\nu$ (photon energy) plot and the x -axis ($E = h\nu$) gives the band gap energy of the samples. Figure 6 presents the $[F(R)hv]^n$ vs. $h\nu$ plots for direct ($n = 2$) band gaps.

The direct band gap values were 3.43 eV, 2.68 eV, 2.38 eV, 2.73 eV, and 2.99 eV for TiO₂, NiFe₂O₄, NiFeTi500, NiFeTi600, and NiFeTi700, respectively. The direct band gap of the NiFe₂O₄ and TiO₂ fibers is in good agreement with values reported in the literature⁴²⁻⁴⁵. The gap energies of the NiFe₂O₄/TiO₂ samples were close to the E_g of NiFe₂O₄. Banda, Kurup⁴⁴ reported a similar behavior for NiFe₂O₄@TiO₂ nanoparticles (E_g of NiFe₂O₄@TiO₂ and NiFe₂O₄ were 1.63 eV and 1.67 eV, respectively). More importantly, the E_g of the NiFe₂O₄, NiFeTi500, NiFeTi600, and NiFeTi700 fibers are all within the visible light range, meaning that the catalysts are visible light active under the experimental conditions of the present work. Meanwhile, the E_g of NiFe₂O₄/TiO₂ fibers increased from 2.38 eV to 2.99 eV as the calcination temperature rose from 500 °C to 700 °C, indicating that E_g is sensitive to temperature. The narrow band gaps of the NiFe₂O₄/TiO₂ fibers facilitate electronic transitions by visible light irradiation, making this novel material promising for photocatalytic applications⁶.

To build an intrinsic mechanism and understand better the proposed photocatalytic system, band edge positions of TiO₂ and NiFe₂O₄ fibers were deduced using Equations 2 and 3.

$$E_{CB} = \chi - E^C - 0.5E_g \quad (2)$$

$$E_{VB} = E_{CB} + E_g \quad (3)$$

where, E_{CB} and E_{VB} are the respective CB and VB potentials, χ is the absolute electronegativity, E^C represents the energy of free electrons on the hydrogen scale (~4.5 eV), and E_g is the band gap energy of the semiconductor, calculated above. Herein, χ values for NiFe₂O₄ and TiO₂ were 4.65 and 5.8 eV, respectively. These values were taken from references^{44,46}.

The E_{CB} values of TiO₂ and NiFe₂O₄ were -0.415 eV and -0.815 eV, while E_{VB} values were 3.015 eV and 1.115 eV, respectively. Based on these edge band potentials, band gaps, and the experimental observations, a mechanism was later proposed to explain the photocatalytic degradation of Congo red and crystal violet dyes in the presence of NiFe₂O₄/TiO₂ fibers and visible light.

3.1. Photocatalytic experiments

Figure 7 shows the decolorization efficiency (C/C_0) of the fibers against Crystal violet (CV) (Figure 7a) and Congo red (CR) (Figure 7b) dyes. After 300 minutes of testing with the CV dye, the TiO₂, NiFeTi500, NiFeTi600, and NiFeTi700

fibers showed photodegradation of 74%, 72%, 75%, and 77%, respectively. The performance of the NiFe₂O₄/TiO₂ was relatively the same as that presented by the TiO₂ fibers alone. On the other hand, for CR dye, after 30 minutes, the same fibers showed 13%, 87%, 77%, and 42% degradation, respectively. Clearly, the hybrid NiFe₂O₄/TiO₂ fibers are more efficient at removing the anionic Congo red dye. According to the literature, variations in the pH can modify the electrostatic affinity between dye molecules and the photocatalyst, modulating the photodegradation⁴⁷⁻⁴⁹. The surface of a catalyst tends to negatively adsorb cationic dyes at pHs above the zero-point charge (pHzpc)⁴⁸. Conversely, anionic species will adsorb under conditions of pH below the pHzpc. TiO₂ presents a zero-charge point situated around 6.5, which is close to the pH conditions of the CV and CR solutions prepared in this work. Under such conditions, TiO₂ has a slightly negatively charged surface, leading to some attractive forces with the cationic CV dye. On the other hand, ZPC measures of nickel ferrite have shown a pHzpc around 10⁵⁰, above the pH of the CV solution. Thus, the nickel ferrite fibers have positively charged surfaces that tend to adsorb anionic dyes under the studied pH conditions. This explains the comparable photodegradation efficiency of CV by the TiO₂ and hybrid NiFe₂O₄/TiO₂ fibers. Furthermore, crystal violet is a very difficult dye to degrade. Even under UV light stimulation, a long time is necessary to achieve a significant degradation efficiency. Pawar and Chaudhary⁵¹ applied In₂O₃ nanocapsules to photodegrade crystal violet dye using sunlight. They achieved a photodegradation efficiency of 90% after 3 h of sunlight irradiation. TiO₂ nanotubes were reported to remove about 95% of crystal violet after 6 h of UV light irradiation⁴⁹. Gd-doped bismuth ferrite nanoparticles showed an 85% photodegradation efficiency of CV dye under 3 h of visible light irradiation⁵².

On the other hand, the highly efficient CR removal after only 30 min may result from the synergistic adsorptive and photocatalytic processes that might be happening simultaneously in the suspension. The adsorptive effect may have been stimulated by the attraction forces between the anionic sulfonate groups of the dye and the Ni²⁺, Fe³⁺, and Ti⁴⁺ ions on the surface of the samples.

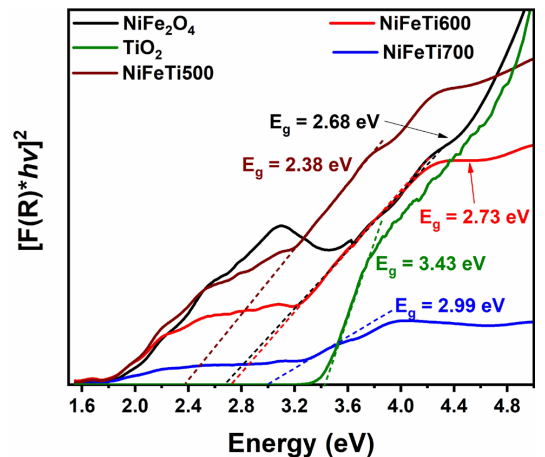


Figure 6. Plots of $[F(R)hv]^n$ vs. $h\nu$ for the TiO₂, NiFe₂O₄, NiFeTi500, NiFeTi600, and NiFeTi700 fibers.

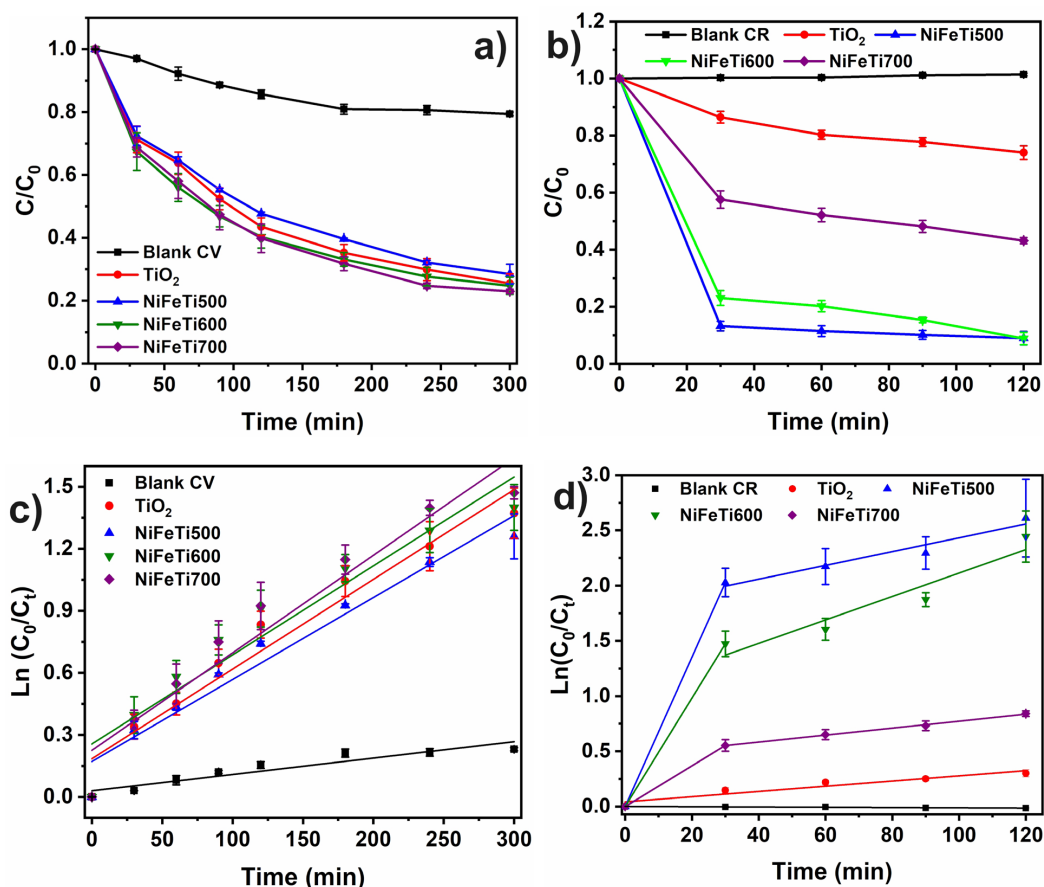


Figure 7. (a) Degradation curves of CV (a) and CR (b) in the systems with fibers under visible light irradiation. (c) Pseudo-first order kinetic curves for CV (c) and CR (d) dyes solution loaded with TiO_2 , NiFeTi500, NiFeTi600, and NiFeTi700 catalysts.

Also, as discussed above, nickel ferrite has a pHzpc of 10; thus, at pH 7 the anionic CR dye will adsorb on the positively charged NiFe_2O_4 surface and contribute to the photocatalytic performance. TiO_2 has less adsorptive influence since its pHzpc is lower than the solution pH. This may explain the low degradation efficiency of the TiO_2 fibers alone. The solutions without the fibers showed no appreciable CR removal in under visible light, indicating little photolysis. However, the blank CV dye solution was decolorized by 14.3% (120 min) and about 20.6% after 300 min of visible light irradiation. This indicates that this dye is less stable than CR under the experimental conditions. The results show the efficiency of SBS-synthesized Ni-ferrite/ TiO_2 fibers in the decolorization of CR, which is comparable or even superior to the removal by other photocatalysts, such as $\text{NiFe}_2\text{O}_4/\text{ZnO}$ hybrids (95% under simulated sunlight for 10 min)⁸, CoFe_2O_4 (84-92% after UV/Vis irradiation for 100 min and pH=9)⁵³, and $\text{Cu}_x\text{Mg}_{0.82-x}\text{Fe}_2\text{O}_4$ (80% under UV light radiation for 330 min at pH=8)⁵⁴.

To further analyze the interaction between the Ni-ferrite/ TiO_2 fibers and the dyes, the pseudo-first-order kinetic model was applied according to the equation:

$$\ln\left(\frac{C_0}{C_t}\right) = k_{app}t \quad (4)$$

where C_0 is the initial concentration of CV or CR aqueous solution, C_t is the dye concentration in the solutions after a given irradiation time, and k_{app} is the apparent rate constant¹¹.

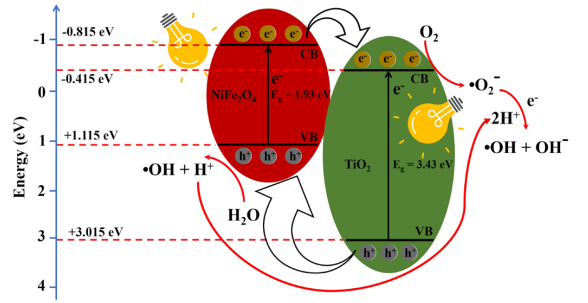
The plots of $\ln(C_0/C_t)$ versus reaction time (Figure 7c and 7d) show a reasonable linear fitting (R^2) for the CV/ $\text{NiFe}_2\text{O}_4/\text{TiO}_2$ and CR/ $\text{NiFe}_2\text{O}_4/\text{TiO}_2$ systems, with R^2 ranging from 0.89 to 0.96, and 0.91 to 0.99 (Table 4), respectively. The initial apparent reaction rate constant (k_i) for the photocatalysis of CV dye was 0.0043, 0.004, 0.0043, and 0.0047 min^{-1} and for CR was 0.0024, 0.0676, 0.0491, and 0.0184 min^{-1} for TiO_2 , NiFeTi500, NiFeTi600, and NiFeTi700 fibers, respectively. The $\text{NiFe}_2\text{O}_4/\text{TiO}_2$ hybrid fibers tended to show superior CV and CR decolorization than the isolated TiO_2 fibers. However, the high decolorization kinetics did not persist after 30 min of reaction. Therefore, after 30 min, the recorded reaction rates (k_2) were lower, falling between 0.0031 to 0.0106 min^{-1} for CR. The lower k_2 values may have resulted from the high initial decolorization rate, with a fast dye removal in the first 30 min that decreased the available CR dye in the solution. The k_{app} found in this work is comparable and sometimes superior to the reported for CoFe_2O_4 nanoparticles ($k = 0.006\text{-}0.006 \text{ min}^{-1}$, under UV irradiation, $C_0 = 10 \text{ mg/L}$, $m = 10 \text{ mg}$)⁵³, $\text{Co}_3\text{O}_4/\text{TiO}_2/\text{GO}$ nanoparticles ($k = 0.016\text{-}0.028 \text{ min}^{-1}$, under simulated solar light, $C_0 = 10 \text{ mg/L}$, $m = 50 \text{ mg}$)⁵⁵, ZnO/activated carbon

Table 4. Pseudo-first order kinetic constants (k) and correlation coefficients (R²) for the degradation of CV and CR dye under visible light irradiation.

Samples	Visible light		
	Pseudo-first order		
	k ₁ (min ⁻¹)	k ₂ (min ⁻¹)	R ²
CV Blank	0.00079	-	0.89
CV + TiO ₂	0.00434	-	0.95
CV + NiFeTi500	0.00396	-	0.96
CV + NiFeTi600	0.0043	-	0.92
CV + NiFeTi700	0.00471	-	0.94
CR Blank	-	-	-
CR + TiO ₂	0.00236	-	0.91
CR + NiFeTi500	0.06758	0.00624	0.95
CR + NiFeTi600	0.04907	0.01062	0.91
CR + NiFeTi700	0.01843	0.00314	0.99

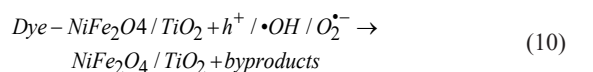
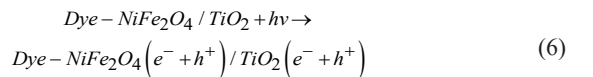
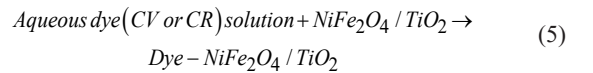
nanomaterials ($k = 0.005\text{-}0.051 \text{ min}^{-1}$, under solar light, $C_0 = 3.0 \times 10^{-4} \text{ mol/dm}^3$, $m = 50 \text{ mg}$)⁵⁶, NiFe₂O₄/multi-walled carbon nanotubes ($k = 0.014 \text{ min}^{-1}$, simulated solar light, $C_0 = 20 \text{ mg/L}$, $m = 80 \text{ mg}$)⁵⁷, and similar to rates presented by NiFe₂O₄/ZnO hybrids ($k = 0.033\text{-}0.114 \text{ min}^{-1}$, simulated sunlight, $C_0 = 20 \text{ mg/L}$, $m = 50 \text{ mg}$)⁸. All these works used either a higher catalyst dosage or lower initial concentration than that used in the present work, further confirming the significance of our results.

A plausible photocatalytic mechanism of Congo red and crystal violet in the presence of the NiFe₂O₄/TiO₂ hybrid fibers was proposed (Figure 8). The CV or CR molecules dispersed in the aqueous solutions adsorb onto the surface of the NiFe₂O₄/TiO₂ fibers⁵⁸ (Equation 5), leading to the dye-sensitization of the TiO₂ on the hybrid⁵⁹. Visible light irradiation promotes the excitation of electrons (e^-) from the valence band (VB) to the conduction band (CB) of the dye-sensitized TiO₂ and NiFe₂O₄ fibers, generating the same amount of electron holes (h^+) in the VB⁴⁴ (Equation 6). At local interface regions between fibers, electrons photogenerated from the CB of NiFe₂O₄ quickly moves to the CB of TiO₂ with a synchronous movement of photogenerated holes from the VB of TiO₂ to the VB of NiFe₂O₄, as schematized in Figure 8. This phenomenon is ascribed to the higher negative CB potential of NiFe₂O₄ (-0.815 eV) than that of TiO₂ (-0.415 eV). Besides, TiO₂ has a higher positive VB edge potential (+3.015 eV) than NiFe₂O₄ (+1.115 eV). Therefore, the synergistic combination between the visible light active NiFe₂O₄ and UV light active TiO₂ produced a hybrid material with a band structure that prevents e^-/h^+ recombination as it favors e^- transfer from NiFe₂O₄ to TiO₂. The photoinduced electrons and holes can, thus, more effectively participate in the free radical generation, which is fundamental for the degradation of organic dyes. According to the literature⁸, the oxygen dissolved in the aqueous solution scavenges electrons, yielding the formation of active free radicals ($\bullet\text{OH}$, $\text{O}_2^{\bullet-}$) (Equations 7 and 8). On the other hand, electron donors (H_2O) will react with the photoproduced holes to yield active $\bullet\text{OH}$ ⁶⁰ (Equation 9). The degradation

**Figure 8.** Schematic photodegradation mechanism of CR and CV dyes by NiFe₂O₄/TiO₂ fibers.

process occurs when the generated holes and free radicals attack the surface-adsorbed dye molecules (Equation 10).

In basic photocatalytic mechanism the following equations are involved:



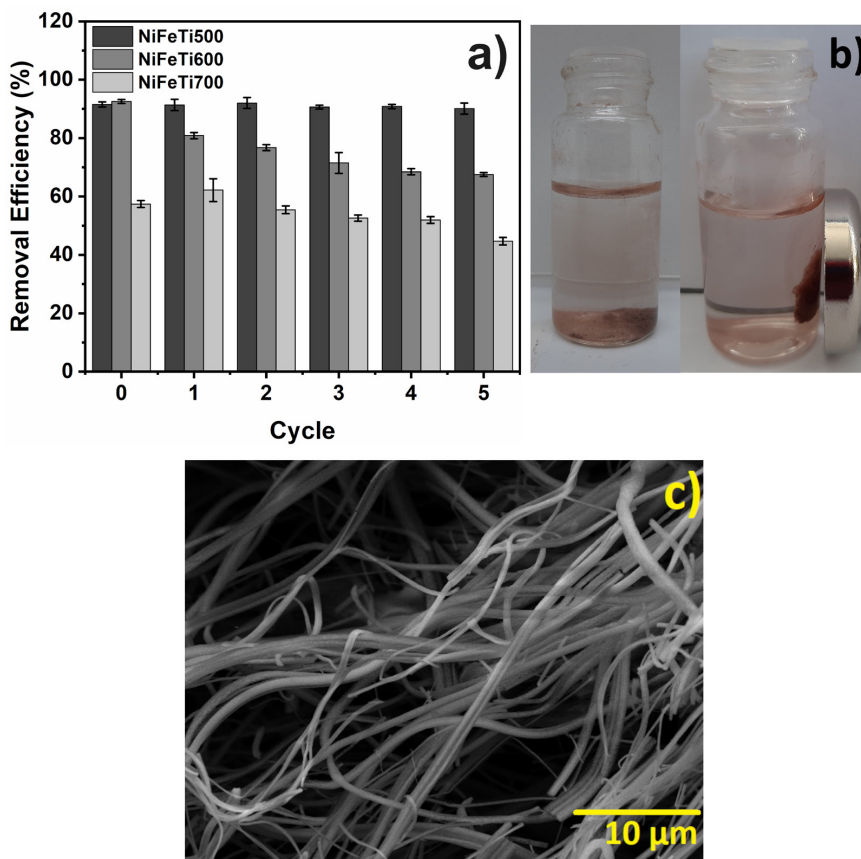


Figure 9. (a) Recycling results of the $\text{NiFe}_2\text{O}_4/\text{TiO}_2$ fibers calcined at 500 °C. (b) Magnetic NiFeTi500 hybrid fibers in a decolorized CR solution. (c) NiFeTi500 fibers after 5 cycles of photocatalytic experiments and recovery.

3.2. Recyclability and stability studies

The recyclability of photocatalysts is one of the crucial parameters for developing practical photocatalytic systems. To evaluate the recyclability of the $\text{NiFe}_2\text{O}_4/\text{TiO}_2$ fibers, after each experiment using CR dye, the fibers were collected and annealed at 400 °C. After that, the recovered fibers were subjected to new cycles of CR photodegradation studies. Figure 9a, b shows the recyclability results for the NiFeTi500, NiFeTi600, and NiFeTi700 compositions. The CR removal efficiency by the NiFeTi500 sample remains roughly the same after five recycling cycles. Overall, the fibers calcined at 600 and 700 °C showed a reduction in CR removal properties in the first and second recycling cycles. However, the removal efficiency stabilizes above 50% in further cycles. As the samples show good magnetic behavior, they can be easily separated using a magnet, as shown in Figure 9b. The recovered fibers maintain their overall fibrillar morphology after 5 photodegradation experiments (Figure 9c). This indicates that fiber breakage was minimized during experiments and did not affect the photocatalytic/adsorptive results. Overall, the $\text{NiFe}_2\text{O}_4/\text{TiO}_2$ photocatalytic systems developed in this work present high removal efficiencies and can be reused several times. Therefore, this novel material shows potential for application in dye-contaminated waters.

4. Conclusion

In summary, magnetically recoverable $\text{NiFe}_2\text{O}_4/\text{TiO}_2$ hybrid fibers presenting high photocatalytic efficiencies against Crystal violet and Congo red dyes were synthesized by a simultaneous solution blow spinning method. The magnetic behavior suggests that the hybrid material could be easily separated from the aqueous media. The $\text{NiFe}_2\text{O}_4/\text{TiO}_2$ hybrid fibers showed efficient photocatalytic removal of Crystal violet (77%) and Congo red (87%) dye after 300 min and 30 min of visible light irradiation, respectively. The presence of positive charges (Ni^{2+} , Fe^{3+} , and Ti^{4+}) contributed to the improved photocatalytic behavior of the fibers. The degradation process involved electron-hole pair formation upon light irradiation that participated in free $\cdot\text{OH}$ radical formation to attack the surface-adsorbed dye molecules. The recyclability experiments showed that the fibers presented stable Congo red removal efficiency after 5 recycling cycles.

5. Acknowledgments

The authors would like to thank the Coordenação de Aperfeiçoamento de Pessoal de Nível Superior (CAPES) fellowship - Finance Code 001 (scholarship granted to for the student Hellen C. T. Firmino) and the National Council for Scientific and Technological Development – CNPq (grant nos. 420004/2018-1, and 309771/2021-8) for the financial support.

The authors further acknowledge the following grants/projects: <https://doi.org/10.54499/2020.02797.CEECIND/CP1589/CT0030>, <http://doi.org/10.54499/PTDC/CTM-CTM/2156/2020>, <https://doi.org/10.54499/2022.02498.PTDC>, <https://doi.org/10.54499/UIDB/00481/2020>, and <https://doi.org/10.54499/UIDP/00481/2020> from Fundação para a Ciência e a Tecnologia (FCT), and CENTRO-01-0145-FEDER-022083 from Centro Portugal Regional Operational Programme (Centro2020), under the PORTUGAL 2020 Partnership Agreement, through the European Regional Development Fund (ERDF). This study was also financed in part by the Coordenação de Aperfeiçoamento de Pessoal de Nível Superior - Brasil (CAPES) - Finance Code 001.

6. References

- Sharma S, Bhattacharya A. Drinking water contamination and treatment techniques. *Appl Water Sci.* 2017;7(3):1043-67.
- Manea YK, Khan AM, Nabi SA. Facile synthesis of Mesoporous Sm@POA/TP and POA/TP nanocomposites with excellent performance for the photocatalytic degradation of MB and MG dyes. *J Alloys Compd.* 2019;791:1046-62.
- Tariq N, Fatima R, Zulfiqar S, Rahman A, Warsi MF, Shakir I. Synthesis and characterization of MoO₃/CoFe₂O₄ nanocomposite for photocatalytic applications. *Ceram Int.* 2020;46(13):21596-603.
- Yeap KL, Teng TT, Poh BT, Morad N, Lee KE. Preparation and characterization of coagulation/flocculation behavior of a novel inorganic-organic hybrid polymer for reactive and disperse dyes removal. *Chem Eng J.* 2014;243:305-14.
- Liu M, Yin W, Zhao T-L, Yao Q-Z, Fu S-Q, Zhou G-T. High-efficient removal of organic dyes from model wastewater using Mg(OH)₂-MnO₂ nanocomposite: synergistic effects of adsorption, precipitation, and photodegradation. *Separ Purif Tech.* 2021;272:118901.
- Araujo R, Nascimento E, Firmino H, Macedo D, Neves G, Morales M, et al. α -Fe₂O₃ fibers: an efficient photocatalyst for dye degradation under visible light. *J Alloys Compd.* 2021;882(15):160683.
- Zhu H, Jiang R, Li J, Fu Y, Jiang S, Yao J. Magnetically recyclable Fe₃O₄/Bi₂S₃ microspheres for effective removal of Congo red dye by simultaneous adsorption and photocatalytic regeneration. *Separ Purif Tech.* 2017;179:184-93.
- Zhu H-Y, Jiang R, Fu Y-Q, Li R-R, Yao J, Jiang S-T. Novel multifunctional NiFe₂O₄/ZnO hybrids for dye removal by adsorption, photocatalysis and magnetic separation. *Appl Surf Sci.* 2016;369:1-10.
- Harifi T, Montazer M. A novel magnetic reusable nanocomposite with enhanced photocatalytic activities for dye degradation. *Separ Purif Tech.* 2014;134:210-9.
- Baig MM, Zulfiqar S, Yousuf MA, Touqeer M, Ullah S, Agboola P, et al. Structural and photocatalytic properties of new rare earth La³⁺ substituted MnFe₂O₄ ferrite nanoparticles. *Ceram Int.* 2020;46(14):23208-17.
- Amulya MS, Nagaswarupa H, Kumar MA, Ravikumar C, Kusuma K. Sonochemical synthesis of MnFe₂O₄ nanoparticles and their electrochemical and photocatalytic properties. *J Phys Chem Solids.* 2021;148:109661.
- Revathi J, Abel MJ, Archana V, Sumithra T, Thiruneelakandan R, Prince JJ. Synthesis and characterization of CoFe₂O₄ and Ni-doped CoFe₂O₄ nanoparticles by chemical Co-precipitation technique for photo-degradation of organic dyestuffs under direct sunlight. *Physica B.* 2020;587:412136.
- Wang J, Asakura Y, Yin S. Preparation of (Zn_{1-x}Ge)(N₂Ox) nanoparticles with enhanced NOx decomposition activity under visible light irradiation by nitridation of Zn₃GeO₈ nanoparticles designed precisely. *Nanoscale.* 2019;11(42):20151-60.
- Asakura Y, Inaguma Y, Ueda K, Masubuchi Y, Yin S. Synthesis of gallium oxynitride nanoparticles through hydrothermal reaction in the presence of acetylene black and their photocatalytic NOx decomposition. *Nanoscale.* 2018;10(4):1837-44.
- Wang J, Asakura Y, Hasegawa T, Yin S. High-concentration N-doped La₂Ti₂O₇ nanocrystals: effects of nano-structuration and doping sites on enhancing the photocatalytic activity. *Chem Eng J.* 2021;423:130220.
- Sohail M, Xue H, Jiao Q, Li H, Khan K, Wang S, et al. Synthesis of well-dispersed TiO₂/CNTs@CoFe₂O₄ nanocomposites and their photocatalytic properties. *Mater Res Bull.* 2018;101:83-9.
- Manohar A, Chintagumpala K, Kim KH. Mixed Zn-Ni spinel ferrites: structure, magnetic hyperthermia and photocatalytic properties. *Ceram Int.* 2021;47(5):7052-61.
- Dojcinovic MP, Vasiljevic ZZ, Pavlovic VP, Barisic D, Pajic D, Tadic NB, et al. Mixed Mg-Co spinel ferrites: structure, morphology, magnetic and photocatalytic properties. *J Alloys Compd.* 2021;855:157429.
- Bhat SA, Zafar F, Mondal AH, Kareem A, Mirza AU, Khan S, et al. Photocatalytic degradation of carcinogenic Congo red dye in aqueous solution, antioxidant activity and bactericidal effect of NiO nanoparticles. *J Iran Chem Soc.* 2020;17(1):215-27.
- Tariq A, Gull M, Shaikh A, Hussain S, Hussain R, Haq S, et al. Grafting the ferrites of cobalt and zinc on MWCNTs for adsorption of crystal violet. *Int J Environ Sci Technol.* 2023;20(11):12465.
- Mani S, Bharagava RN. Exposure to crystal violet, its toxic, genotoxic and carcinogenic effects on environment and its degradation and detoxification for environmental safety. *Rev Environ Contam Toxicol.* 2016;237:71-104.
- Medeiros ES, Glenn GM, Klamczynski AP, Orts WJ, Mattoso LH. Solution blow spinning: a new method to produce micro- and nanofibers from polymer solutions. *J Appl Polym Sci.* 2009;113(4):2322-30.
- Firmino HC, Nascimento EP, Bonan RF, Maciel PP, Castellano LR, Santana LN, et al. Antifungal activity of TiO₂-CeO₂ nanofibers against *Candida fungi*. *Mater Lett.* 2021;283:128709.
- Nascimento EP, Firmino HC, Santos AM, Sales HB, Silva VD, Macedo DA, et al. Facile synthesis of hollow F-doped SnO₂ nanofibers and their efficiency in ethanol sensing. *J Am Ceram Soc.* 2021;104(3):1297-308.
- Nascimento EP, Araujo RN, Firmino HC, Mastelaro VR, Loureiro FJ, Neves GA, et al. Parallel-solution blow spun Al-SnO₂/F-SnO₂ fibers as an efficient room temperature ethanol sensor. *Ceram Int.* 2022;48(9):13163-74.
- Santos A, Mota M, Leite R, Neves G, Medeiros E, Menezes R. Solution blow spun titania nanofibers from solutions of high inorganic/organic precursor ratio. *Ceram Int.* 2018;44(2):1681-9.
- Byrne C, Fagan R, Hinder S, McCormack DE, Pillai SC. New approach of modifying the anatase to rutile transition temperature in TiO₂ photocatalysts. *RSC Advances.* 2016;6(97):95232-8.
- Sivakumar P, Ramesh R, Ramanand A, Ponnusamy S, Muthamizhchelvan C. Preparation and properties of nickel ferrite (NiFe₂O₄) nanoparticles via sol-gel auto-combustion method. *Mater Res Bull.* 2011;46(12):2204-7.
- Shebanova ON, Lazor P. Raman spectroscopic study of magnetite (FeFe₂O₄): a new assignment for the vibrational spectrum. *J Solid State Chem.* 2003;174(2):424-30.
- Yadav RS, Kufitka I, Vilcakova J, Havlicka J, Masilkov J, Kalina L, et al. Structural, magnetic, dielectric, and electrical properties of NiFe₂O₄ spinel ferrite nanoparticles prepared by honey-mediated sol-gel combustion. *J Phys Chem Solids.* 2017;107:150-61.
- Ma H, Yang J, Dai Y, Zhang Y, Lu B, Ma G. Raman study of phase transformation of TiO₂ rutile single crystal irradiated by infrared femtosecond laser. *Appl Surf Sci.* 2007;253(18):7497-500.
- Chamritski I, Burns G. Infrared-and Raman-active phonons of magnetite, maghemite, and hematite: a computer simulation and spectroscopic study. *J Phys Chem B.* 2005;109(11):4965-8.

33. Yadav RS, Havlica J, Masilko J, Kalina L, Wasserbauer J, Hajdúchová M, et al. Effects of annealing temperature variation on the evolution of structural and magnetic properties of NiFe₂O₄ nanoparticles synthesized by starch-assisted sol-gel auto-combustion method. *J Magn Magn Mater*. 2015;394:439-47.
34. Ahlawat A, Sathé V, Reddy V, Gupta A. Mossbauer, Raman and X-ray diffraction studies of superparamagnetic NiFe₂O₄ nanoparticles prepared by sol-gel auto-combustion method. *J Magn Magn Mater*. 2011;323(15):2049-54.
35. Kumar P, Rana G, Dixit G, Kumar A, Sharma V, Goyal R, et al. Structural, electrical and magnetic properties of dilutely Y doped NiFe₂O₄ nanoparticles. *J Alloys Compd*. 2016;685:492-7.
36. Mantilla J, Félix LL, Martínez M, Souza P, Rodrigues P, Figueiredo L, et al. Evidence of surface spin-glass behavior in NiFe₂O₄ nanoparticles determined using magnetic resonance technique. *J Magn Magn Mater*. 2019;476:392-7.
37. Faria DL, Silva SV, Oliveira M. Raman microspectroscopy of some iron oxides and oxyhydroxides. *J Raman Spectrosc*. 1997;28(11):873-8.
38. Cullity BD, Graham CD. Introduction to magnetic materials. Hoboken: John Wiley & Sons; 2011.
39. Şabikoğlu İ, Paralı L, Malina O, Novak P, Kaslik J, Tucek J, et al. The effect of neodymium substitution on the structural and magnetic properties of nickel ferrite. *Prog Nat Sci*. 2015;25(3):215-21.
40. Ushakov M, Senthilkumar B, Selvan RK, Felner I, Oshtrakh M. Mössbauer spectroscopy of NiFe₂O₄ nanoparticles: the effect of Ni²⁺ in the Fe³⁺ local microenvironment in both tetrahedral and octahedral sites. *Mater Chem Phys*. 2017;202:159-68.
41. Joshi S, Kumar M, Pandey H, Singh M, Pal P. Structural, magnetic and dielectric properties of Gd³⁺ substituted NiFe₂O₄ nanoparticles. *J Alloys Compd*. 2018;768:287-97.
42. Joshi S, Kumar M, Chhoker S, Srivastava G, Jewariya M, Singh V. Structural, magnetic, dielectric and optical properties of nickel ferrite nanoparticles synthesized by co-precipitation method. *J Mol Struct*. 2014;1076:55-62.
43. Hoseini SA, Khademolhoseini S. Investigation of the structural, optical and magnetic properties of nickel ferrite nanoparticles synthesized through modified sol-gel method. *J Mater Sci Mater Electron*. 2016;27(6):5943-7.
44. Banda PG, Kurup GB, Mucherla R. Immobilization of Ag nanoparticles on NiFe₂O₄@TiO₂@PDA: multifunctional catalytic action toward the reduction of 4-Nitrophenol and photodegradation of methylene blue and ciprofloxacin. *J Phys Chem Solids*. 2023;181:111556.
45. Sukumar M, Rajabathar JR, Hamad A-L, Suresh S, Dash CS, Sundararajan M, et al. Synthesize and characterization of copper doped nickel ferrite nanoparticles effect on magnetic properties and visible light catalysis for rhodamine dye degradation mechanism. *J Alloys Compd*. 2023;953:169902.
46. Babu B, Koutavarapu R, Shim J, Kim J, Yoo K. Improved sunlight-driven photocatalytic abatement of tetracycline and photoelectrocatalytic water oxidation by tin oxide quantum dots anchored on nickel ferrite nanoplates. *J Electroanal Chem*. 2021;900:115699.
47. Lin TH, An H, Nam NTH, Hai ND, Binh TLN, Cong CQ, et al. Magnesium ferrite/titanium dioxide/reduced graphene oxide composite photocatalyst for degradation of crystal violet under ultraviolet irradiation. *Mater Chem Phys*. 2023;301:127661.
48. Liao Y-HB, Wang JX, Lin J-S, Chung W-H, Lin W-Y, Chen C-C. Synthesis, photocatalytic activities and degradation mechanism of Bi₂WO₆ toward crystal violet dye. *Catal Today*. 2011;174(1):148-59.
49. Mohanty S, Moullick S, Maji SK. Adsorption/photodegradation of crystal violet (basic dye) from aqueous solution by hydrothermally synthesized titanate nanotube (TNT). *J Water Process Eng*. 2020;37:101428.
50. Barale M, Lefèvre G, Carrette F, Catalette H, Fédoroff M, Cote G. Effect of the adsorption of lithium and borate species on the zeta potential of particles of cobalt ferrite, nickel ferrite, and magnetite. *J Colloid Interface Sci*. 2008;328(1):34-40.
51. Pawar KK, Chaudhary LS, Mali SS, Bhat TS, Sheikh AD, Hong CK, et al. In₂O₃ nanocapsules for rapid photodegradation of crystal violet dye under sunlight. *J Colloid Interface Sci*. 2020;561:287-97.
52. Kossar S, Banu IS, Aman N, Amiruddin R. Investigation on photocatalytic degradation of crystal violet dye using bismuth ferrite nanoparticles. *J Dispers Sci Technol*. 2020;42(14):1-10.
53. Ali N, Said A, Ali F, Raziq F, Ali Z, Bilal M, et al. Photocatalytic degradation of congo red dye from aqueous environment using cobalt ferrite nanostructures: development, characterization, and photocatalytic performance. *Water Air Soil Pollut*. 2020;231(2):50.
54. Bessy T, Manna C, Johnson J, Hegazy RA, Bindhu M, Florence S. Efficient antibacterial activities and photocatalytic degradation of congo red dye by CuxMg_{0.8-x}Fe₂O₄ nanoparticles synthesized by combustion method. *J Mater Sci Mater Electron*. 2023;34(6):518.
55. Jo W-K, Kumar S, Isaacs MA, Lee AF, Karthikeyan S. Cobalt promoted TiO₂/GO for the photocatalytic degradation of oxytetracycline and Congo Red. *Appl Catal B*. 2017;201:159-68.
56. Raizada P, Singh P, Kumar A, Sharma G, Pare B, Jonnalagadda SB, et al. Solar photocatalytic activity of nano-ZnO supported on activated carbon or brick grain particles: role of adsorption in dye degradation. *Appl Catal A Gen*. 2014;486(22):159-69.
57. Zhu H-Y, Jiang R, Huang S-H, Yao J, Fu F-Q, Li J-B. Novel magnetic NiFe₂O₄/multi-walled carbon nanotubes hybrids: facile synthesis, characterization, and application to the treatment of dyeing wastewater. *Ceram Int*. 2015;41(9):11625-31.
58. Hou X, Feng J, Liu X, Ren Y, Fan Z, Wei T, et al. Synthesis of 3D porous ferromagnetic NiFe₂O₄ and using as novel adsorbent to treat wastewater. *J Colloid Interface Sci*. 2011;362(2):477-85.
59. Pan L, Zou J-J, Zhang X, Wang L. Water-mediated promotion of dye sensitization of TiO₂ under visible light. *J Am Ceram Soc*. 2011;133(26):10000-2.
60. Saini D, Aggarwal R, Sonker AK, Sonkar SK. Photodegradation of azo dyes in sunlight promoted by nitrogen-sulfur-phosphorus codoped carbon dots. *ACS Appl Nano Mater*. 2021;4(9):9303-12.